A Pressure- or Velocity-Dependent Acceleration Rate Law for the Shock-to-Detonation Transition Process in PBX 9502 High Explosive

Scott I. Jackson

Shock and Detonation Physics (M-9)
Los Alamos National Laboratory
Los Alamos, NM 87545 USA

Abstract

Shock-to-detonation transition profiles of PBX 9502 explosive are analyzed to develop a rate law for shock acceleration. The shock motion profiles are seen to follow a common trend in the shock acceleration–velocity frame, aside from an early time transient that is dependent on the initiating shock strength. The duration of the early time transient is seen to correlate with the initial shock strength. The common shock acceleration profile is seen to be Arrhenius-like with respect to the local particle velocity or pressure. A dual-rate pressure-dependent Arrhenius-type rate law is developed with the duration of the early rate set by the initial shock strength. The rate law is able to predict the shock motion for all tests well in both particle velocity and pressure space. In addition to directly measuring commonalities in the acceleration profiles of the experimental shock motion, this work provides insight into the functional form of the reaction rate laws for this TATB-based high explosive. The rate law also supports the concept that shock-driven reaction in heterogenous high explosives is driven by localized ignition and growth of hotspots.

Keywords: detonation, Shock-to-Detonation Transition, SDT, detonation reaction rate, high explosive

*LA-UR-19-28536
**Published article: https://doi.org/10.1016/j.combustflame.2019.11.036
Email address: sjackson@lanl.gov (Scott I. Jackson)

1. Introduction

The detonation reaction rate constitutes a key element of reactive models used to predict detonation in high explosives. These reactive models resolve the combustion reaction and require this relation along with an explosive reactant equation of state (EOS) and product EOS as the minimum explosive property data necessary for accurate predictions. Phenomenologically accurate forms for each of these relationships provides better predictions over a larger range of conditions. The extreme properties and short timescales associated with the reaction zone in condensed-phase detonation make measurement of these values challenging, but direct measurements of both the reactant EOS and product EOS are possible [1, 2]. However, it is still difficult to resolve the temporally and spatially small scales of the reaction zones for condensed-phase explosives experimentally, which has complicated attempts to develop accurate reaction rate forms. As a result, a wide range of empirical reaction rate forms are currently implemented in models of condensed-phase explosive reaction [3–7].

Due to these measurement limitations, existing rate law forms have been developed in an ad-hoc fashion using qualitative concepts about the detonation reaction rate that have not been directly measured via experiment. The resulting rate laws are generally very complex, requiring many conditional statements or "switches" to activate different rate forms for different reaction regimes. Common forms are inspired by the Arrhenius rate law, pressure dependent power (e.g. P^n) burn rate laws, and growth of a number of localized ignited "hotspot" regions [8]. Temperature-based Arrhenius reaction rates are commonly observed for combustion of gaseous explosive and in condensed-phase explosives undergoing thermal cookoff [9], while pressure-dependent burn rates are observed in deflagrating strands of explosive [10]. However, these rate forms are derived from experiments in condensed-phase explosives reacting at significantly lower pressures, temperatures, and strain rates than occur during detonation. Additionally, hotspot-induced reactions have never been directly observed in solid explosives [11] but instead are implied from indirect observations including shock-to-detonation wave trajectories, the "dead-pressing" of explosives by sub-critical strength shocks, and the sensitization of explosives by the inclusion of small amounts of material with a substantially different acoustic impedance than the base formulation. Thus, the relevance of each mechanism is not clear in regimes approaching those associated with detonation.

It is common to calibrate reaction rate models to measurements of high explosives being initiated in plate impact facilities [3–7]. These data are appealing

for calibration because the trajectories of shock waves in the explosive undergoing the shock-to-detonation (SDT) transition process access a large range of pressures. Additionally, the wave motion is considered to be one-dimensional (1-D), which simplifies calculations. Early Lagrangian analysis highlighted the ability of such measurements to yield the energy release rate when analyzed via conservation of mass, momentum, and energy [12–15], but only used synthetic data to evaluate such an approach and did not identify any global reaction rate forms. Later, Handley [16] smoothed experimental data with assumed product EOS forms to conclude that the reaction rate versus time relationships were bell shaped and did not overlay, through it was noted that the product EOS choice significantly affected the calculation of the reaction rate. Surprisingly, however, very little other work has been done outside of the computational area to analyze if there are any inherent relationships present in the lead shock acceleration trajectory [17, 18]. The form of such relationships could provide insight into the underlying chemical reaction rate laws. Thus, identification of such relationships could serve to both simplify and speed the development of more accurate reaction rate forms.

In this work, new analysis of previously published shock acceleration trajectories from the high explosive PBX 9502 undergoing 1-D SDT are shown to follow a common pathway in the shock velocity–acceleration regime. The Arrhenius plot is used to demonstrate that this relationship is composed of two rates, both of which are Arrhenius-like with respect to the particle velocity or reactant pressure. Both rates are quantified and used to assemble a common acceleration rate law for PBX 9502 undergoing SDT that is able to predict the shock acceleration profile well. This work provides the first analysis of PBX 9502 high explosive SDT data that infers both the form and magnitude of the reaction rate law for PBX 9502 undergoing shock initiation.

2. Prior Experimental Measurements

The high explosive used in this work is PBX 9502. PBX 9502 is a plastic-bonded explosive composed of 95.0 wt. % TATB (2,4,6-triamino-1,3,5-trinitrobenzene) explosive bonded with 5.0 wt. % Kel-F 800, which is a a proprietary name for the thermoplastic chlorofluoropolymer Polychlorotrifluoroethylene or PCTFE [19]. PBX 9502 is an insensitive high explosive with a nominal detonation velocity of 7.8 mm/μs and a failure diameter near 8.0 mm [20]. The explosive microstructure is composite in nature and composed of a series of TATB grains that are coated with the Kel-F polymer and then pressed into a solid form, as reviewed in Gustavsen et al. [21]. The resulting microstructure is heterogenous and affected by

any variations in the constitutive ingredients [22, 23]. Thus, shock-driven reaction in plastic bonded explosives is a complex field of study due to the heterogenous nature of the microstructure.

The shock-to-detonation initiation data used in this analysis is from Gustavsen et al. [21]. The PBX 9502 is initiated in a plate impact experiment as shown in Fig. 1. A two-stage gas gun is used to accelerate a polymer-tipped projectile to ve-

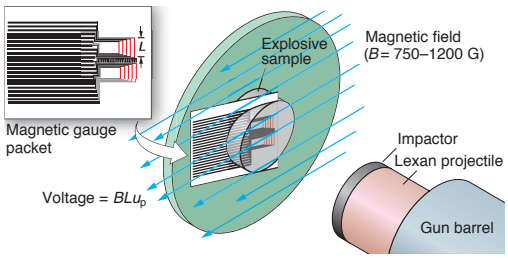

Figure 1: A schematic of the plate impact experiment for SDT measurement from Ref. 24.

locities between 2.3–2.9 mm/μs. The projectile impacts a static explosive target and generates a supported shock wave in the explosive target with impact pressures between 10–16 GPa. The experiment diameter and impactor thickness are sufficient to maintain one-dimensional flow and a supported shock for a significant portion of the SDT process, which can take several microseconds.

The target contains an embedded gauge as a diagnostic to record both the *in situ* post-shock particle velocities and the propagation velocity of the shock wave through the explosive. The gauge package consists of a series of conductors printed onto a 50-μm-thick flexible Fluorinated Ethylene Propylene (FEP) substrate, which is embedded into the target explosive. A second auxiliary gauge is located at the interface between the impactor and target. During the experiment, the gauge package is immersed in a one-dimensional magnetic field of constant strength. Due to the induction effect, any motion of a conductor through the magnetic field induces an electric current in the conductor whose strength is proportional to the relative velocity. As the gauge is embedded inside the sample and of similar impedance, it moves with the particle velocity of the surrounding material. Measurement of the voltage induced in the conductor thus yields the particle velocity history in the explosive [25].

Figure 2 shows particle velocity u_p profiles for the gauges from a plate impact experiment on PBX 9502 to illustrate relevant features of the SDT process. Impact of the Kel-F polymer driver traveling at 2.49 mm/μs induces a 10.65 GPa strength shock in the PBX 9502. The lead (leftmost) gauge at the interface be-

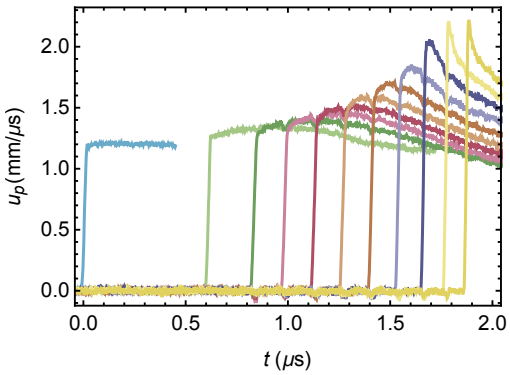

Figure 2: Embedded gauge data for test 2s-69 from Ref. 21.

tween the two materials measures a shock with a postshock velocity of 1.197 $\pm$ 0.025 mm/μs. At this impact condition, the PBX 9502 does not immediately react and the postshock particle velocity remains steady as it is supported by the impactor. Subsequent gauges inside the explosive show increasing lead shock strength that is driven by reactive growth (increasing u_p magnitude shortly behind the shock. The shock wave fully transitions to a detonation between gauges 9 and 10, near 1.67 μs, and assumes a velocity profile that is characteristic of a detonation wave. After transition, the wave shape no longer evolves and the peak particle velocity is constant at approximately 2.2 mm/μs, indicating a von Neumann pressure of at least 29.1 GPa. (Shock interactions between the explosive and the gauge can result in wave impedance effects and possible gauge slip in the explosive, limiting measurement accuracy over timescales less than 50 ns.)

Thus, this diagnostic allows interrogation of the flow inside a polymer or explosive undergoing shock loading. It is particularly valuable for characterizing the entirety of the SDT process in a single test while providing both shock velocity and particle velocity history of the flow. Other methods, such as wedge tests or cutback-style testing, can only provide a subset of this data with each experiment.

3. Analysis

Analytic description of the shock-to-detonation relationship in high explosives has proved difficult to characterize, with relatively little work on the topic and heavy reliance on numerical modeling instead [8]. Winter et al. [17] demonstrated that the shock acceleration profiles for an HMX-based explosive formulation could be collapsed to a single curve when each test was appropriately nondi-

mensionalized by test-specific parameters including the particle velocity immediately behind the initial shock $u_{p,0}$, the Chapman-Jouguet (CJ) particle velocity associated with the sonic surface in a one-dimensional detonation, and the time to detonation t_p from initial shock loading [26]. Similar scaling was seen for the reactive growth peak following the shock arrival as well. However, they were not able to extend this scaling to a TATB-based explosive, possibly due to uncertainties in the CJ particle velocity [18].

In this section, an alternate approach is utilized to characterize shock wave acceleration during the SDT process for PBX 9502. Analysis in velocity-acceleration space is seen to yield commonalities across all tests without the need to introduce any test-specific nondimensionalization factors. Arrhenius theory can then be used to quantify the observed relationship.

3.1. Shock Acceleration Trend

The data of Gustavsen et al. [21] was analyzed to extract the particle velocity associated with the lead shock arrival at each gauge. These values were selected by inspection of each gauge record with selection criteria being the termination of the extremely high slope region associated with the shock front as shown in Fig. 3 for the same data as Fig. 2. Shock fronts with a lead shock particle velocities

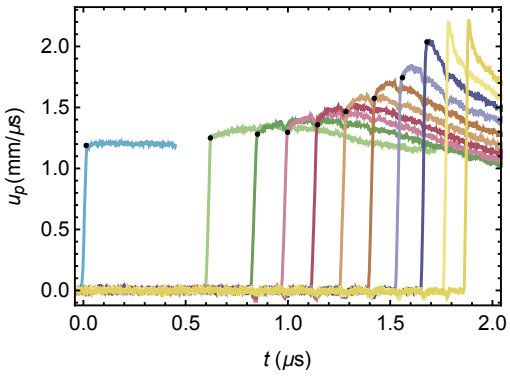

Figure 3: Data from Fig. 2 with lead shock u_p values indicated by black points.

exceeding 2.0 mm/μs were not included in the following analysis as they had profiles that were characteristic of detonation or were past the SDT transition distance as specified by Gustavsen et al. [21].

All 20 of the supported shock experiments from Gustavsen et al. [21] were processed in this manner and the particle velocity versus time profiles for the

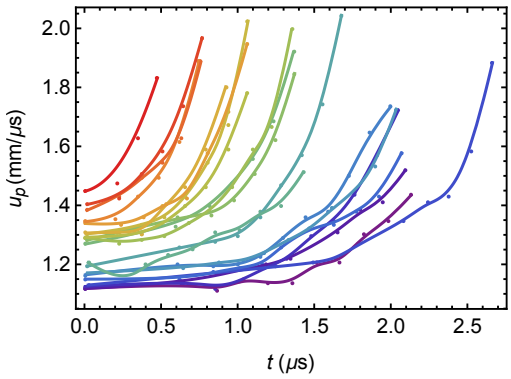

Figure 4: Lead shock u_p points for each test with spline fit curves. Blue-to-red color indicates increasing initial u_p value.

shock front are shown as points in Fig. 4. The color of each test from blue-to-red indicates increasing initial particle velocity $u_{p,0}$ at the impact location. The curves of matching color are spline fits to the shock motion for each individual test. The particle velocity trend is seen to generally monotonically increase with time for each test except at early times for the lower velocity (purple and blue) data. Deviations from the trend in this region are attributed to experimental noise, which is seen to be $\pm$ 0.025 mm/μs or approximately $\pm$ 2.0–2.5% for gauges near the impact location (Fig. 3).

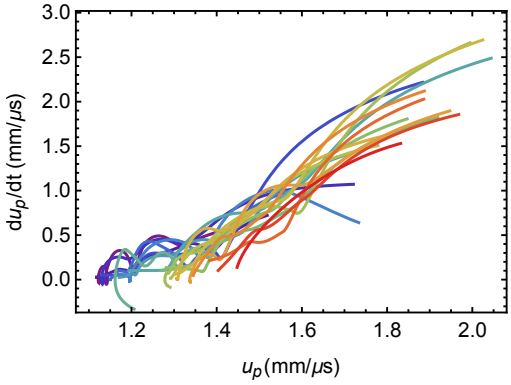

Figure 5: Lead particle velocity versus lead particle acceleration. Blue-to-red color indicates increasing initial u_p value.

All of the velocity-time profiles in Fig. 4 appear to follow a similar trend. Figure 5 shows the derivative of the spline fits $du_p/dt = \dot{u}_p$ versus u_p. The latter

stages of the acceleration data appear to scale well with u_p despite the significant scatter present, which is likely associated with the differentiation of discrete data. However, the early time data for each test appear to be dependent on the initial conditions. Figure 6 replots the data in the format of an Arrhenius plot with $\ln(\dot{u}_p)$ versus $1/u_p$ on the horizontal axis. The shock acceleration profiles all exhibit a

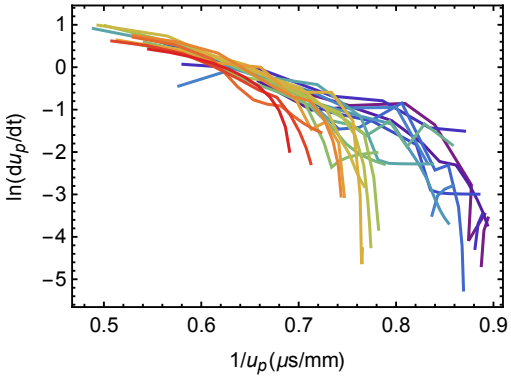

Figure 6: The data of Fig. 5 plotted in the format of an Arrhenius plot. Blue-to-red color indicates increasing initial u_p value.

high negative slope for (early time) higher $1/u_p$ followed by a lower slope for (later time) lower $1/u_p$ values. Good agreement across all profiles is seen for the portion of the trend with a lower magnitude slope at low $1/u_p$ values (high u_p). Profiles do not overlay when exhibiting the initial high-slope behavior at higher $1/u_p$ but the shapes of the curves in this region appear characteristically similar.

The trend at lower $1/u_p$ appears nearly linear, which for an Arrhenius format plot indicates that the data corresponds to an Arrhenius-type relationship of the form

$$\frac{du_p}{dt} = Ae^{-E_{up}/u_p} \tag{1}$$

where A is the pre-exponential factor and E_{up} can be thought of as an "activation particle velocity" that is functionally equivalent to the activation energy in the temperature-sensitive Arrhenius equation. Curves of the form of Eq. 1 will appear as straight lines on the Arrhenius plot with a slope of $-E_{up}$ and a vertical intercept of $\ln A$. The partial adherence of the experimental data to this trend indicates that the latter stages of the shock acceleration process may be predicted with an equation of similar form as Eq. 1.

While not a thermodynamic quantity, the particle velocity is used in this analysis as it is the quantity that is directly measured by the embedded gauge diagnos-

tic and will not be affected by any subsequent changes to the reactant equation of state calibration. However, u_p can be considered a surrogate for pressure in Eq. 1 as the lead shock points follow the reactant Hugoniot during the SDT process. Thus, pressure can be substituted for u_p using the reactant Hugoniot, available in Gustavsen et al. [21], as is done later in this work.

A similar substitution for the corresponding temperature could be found from a complete equation of state [27], but the use of temperature as a bulk parameter in flows is nonphysical for explosives with heterogenous microstructure. For such materials, the passage of the shock wave would result in local variations in the postshock thermodynamic quantities. With sufficiently large postshock pressures that satisfy hydrodynamic assumptions, pressure would be expected to equilibrate quickly in the subsonic postshock region. Temperature and density variations, however, would likely persist for a longer duration in the reaction zone, as controlled by diffusive and conductive effects.

3.2. Quantification of Acceleration Using the Arrhenius Plot

The trajectory of the SDT profiles on the Arrhenius plot in Fig. 6 indicated that the SDT process appears to have two associated acceleration rate trends, with the shock switching from an inital-condition-dependent lower-acceleration trend to a common higher one after a duration. This section quantifies the time of this rate transition and the parameters for both rates.

The "switchover" time t_s and velocity $u_{p,s}$ when the acceleration trend changes from a low rate to a higher one was manually selected by inspection of the data in Figs. 4 and 6, in particular focusing on the location of the peak second derivative of the curves in Fig. 6. The selected switchover time and particle velocity were found to correlate with the initial postshock particle velocity $u_{p,0}$.

The functional forms of these parameters are not known. For simplicity, $u_{p,s}$ is fit to a linear trend via a least squares fit methodology to find

$$u_{p,s} = (0.052 \pm 0.044) - (0.974 \pm 0.035)\, u_{p,0} \tag{2}$$

with velocity in mm/μs. The $\pm$ values following fitted values throughout the paper indicate the standard error associated with the fit for each parameter. The resulting equation has a negative slope and a positive intercept such that $u_{p,s} - u_{p,0} = 0$ at $u_{p,0}$ = 2.018 mm/μs. This value is just below to the Von Neumann u_p value associated with detonation as noted in the previous section and may indicate that the wave does not exhibit a lower rate period as the initial shock strength approaches that of a self-supported detonation. Fitting a negative exponential

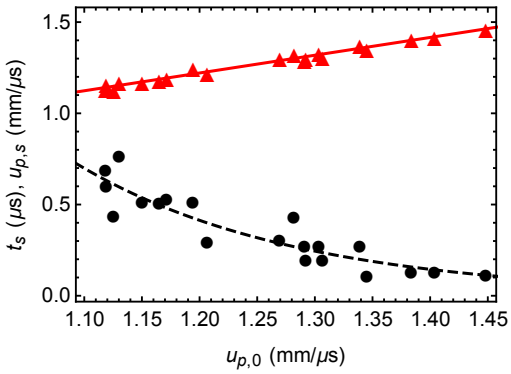

Figure 7: Switchover parameters t_s (black) and $u_{p,s}$ (red) versus $u_{p,0}$.

form to the t_s data also with a least-squares fit methodology yields

$$t_s = (224.1 \pm 181.7)\, e^{(-5.25 \pm 0.69) u_{p,0}} \tag{3}$$

with time and velocity in μs and mm/μs, respectively. The fit reproduces the data trajectory well, goes to zero for large $u_{p,0}$ values and yields a very small t_s values of 5.7 ns at $u_{p,0}$ = 2.018 mm/μs. The data and associated fits are plotted in Fig. 7.

Figures 8 and 9 replot the velocity-time and Arrhenius plots with the selected switchover parameters t_s and $u_{p,s}$ demarcating the two different rate trends as indicated by the change in color. The spline curves in each figure that have been

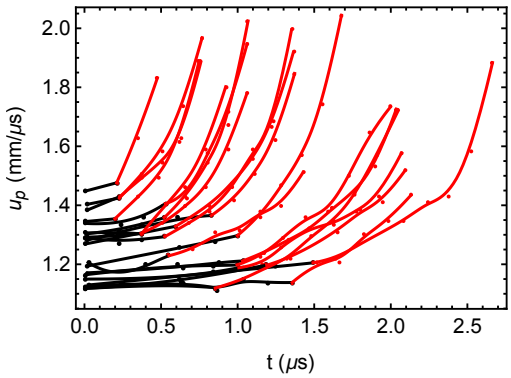

Figure 8: Data of Fig. 5 with colors marking low- (black) and high-rate (red) trends.

separately refit to the low- and high-rate parts of each test to better isolate the trends of each rate. The refitting is seen to not significantly change the trends for each rate.

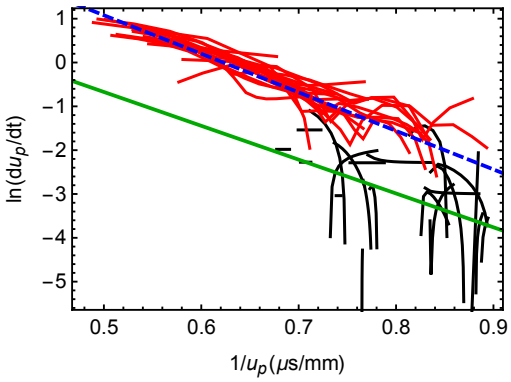

Figure 9: Data of Fig. 6 with colors marking low- (black) and high-rate (red) trends. The straight lines indicate the fits of Eq. 1 to the low- and high-rate curves, respectively.

The high-rate trend (red curves) clearly approximates a line, possibly with slight curvature, in Fig. 9. The data of Fig. 9 was discretized by computing a dataset of $(1/u_p(t), \ln \dot{u}_p(t))$ pairs using the spline fits for each curve and the raw t data associated with each lead shock datapoint as shown in Fig. 4. Equation 1 was then fit to the data with a least-squares fit methodology and by varying parameters A and E_{up} to find $A = 119.5 \pm 18.4$ mm/μs^2 and $E_{up} = 7.69 \pm 0.22$ mm/μs. The resulting standard errors are $\pm$2.9% for E_{up} and $\pm$15.4% for A. The slight curvature could be accounted for with a stretched Arrhenius form, $Ae^{(-E_{up}/u_p)^n}$, but this is not pursued in the present study as good quality predictions are achieved without this additional complexity.

As mentioned, the low-rate trend is more complex to interpret. The experimental noise is on the order of the acceleration magnitude for early times in the SDT process, making differentiation to obtain $\dot{u}_p$ very noisy. Additionally, the resulting profiles do not overlay well. For consistency, the data is assumed to adhere to a similar rate form. Following the same fitting process as with the high-rate data, the low-rate data is fit to obtain $A = 29.3 \pm 21.0$ mm/μs^2 and $E_{up} = 7.72 \pm 1.09$ mm/μs. The resulting standard errors are $\pm$14.1% for E_{up} and $\pm$71.7% for A.

Thus, the E_{up} parameter estimates for the low- and high-rate fits individually have good fit confidence and also overlap to yield a consistent prediction for the activation particle velocity of approximately 7.70 mm/μs. The fit confidence to the pre-exponential A parameter for the high-rate data is good, but the high scatter in the low-rate data gives a poor fit confidence to A. Thus, additional analysis is pursued to better estimate this value.

3.3. Optimizing the low-rate pre-exponential factor

To better optimize the low-rate pre-exponential factor, hereafter referred to as A_L, a shock acceleration rate law is assembled and integrated to fit the u_p–t data of Fig. 4. The fits to the low- and high-rate shock acceleration data are combined in a piecewise equation.

$$\begin{cases} du_p/dt = A_L e^{-E_{up}/u_p} & 0 \leq u_p < u_{p,s} \\ du_p/dt = A_H e^{-E_{up}/u_p} & u_{p,s} \leq u_p \end{cases} \tag{4}$$

The fitting process in the Arrhenius plot format yielded good fits to the high-rate pre-exponential A_H = 119.5 mm/μs^2 and a common activation velocity E_{up} = 7.70 mm/μs. Equation 2 also provides the criteria for the switchover particle velocity $u_{p,s}$. These values are thus used to optimize A_L.

During the optimization process, Equation 4 is combined with the initial condition $u_p(t = 0) = u_{p,0}$ to create an initial value problem for the data from each test i. The error between the resulting solution $f^i(t, u_{p,1}^{i,fit}, A_L)$ for each test and the experimental data points $u_{p,j}^{i,expt}$ is quantified using a merit function of the form:

$$\mathcal{M} = \sum_{i=1}^{20} \sum_{j=1}^{n} \left(u_{p,j}^{i,expt} - f^i(t, u_{p,1}^{i,fit}, A_L) \right)^2 \tag{5}$$

where $u_{p,j}^{i,expt}$ represents the jth experimental post-shock particle velocity point for the ith test. Minimization of $\mathcal{M}$ achieves the best possible fit for A_L across all the tests. For the present experiments, A_L = 19.0 mm/μs^2 yielded the minimum value of $\mathcal{M}$ using the "NMinimize" function in Mathematica, which uses multiple optimization methods in concert to arrive at the minimum merit value. Figure 10 illustrates the sensitivity of A_L, A_H, and E_{up} in Eq. 5 to variations of $\pm 10\%$ off of the values chosen in the present work. Parameter E_{up} is the most sensitive, followed by A_H, with A_L being the least sensitive.

It was previously noted that experimental uncertainty for u_p was approximately $\pm 2.5\%$. In solving for A_L, the $u_{p,1}^i$ values were also allowed to vary in an unconstrained fashion to allow for error in the determination of the lead shock particle velocity. The resulting fitted $u_{p,1}^{i,fit}$ values were found to be within $+2.4\%$ to -3.4% of the measured $u_{p,1}^{i,expt}$ values as shown in Fig. 11, which is consistent with the experimental uncertainty estimate.

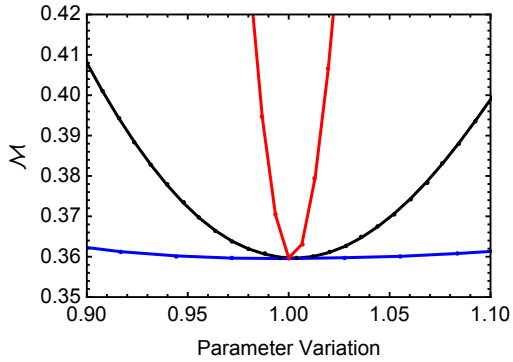

Figure 10: The sensitivity of parameters A_L (blue), A_H (black), Ea (red) in Eq. 5 relative to their optimized values in the text.

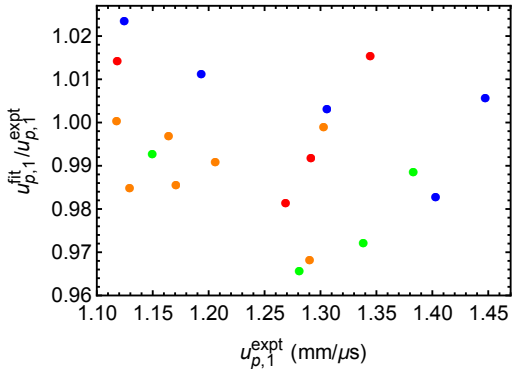

Figure 11: Ratio of fitted and experimental $u_{p,0}$ values. Colors represent explosive lots as discussed in the text.

4. Rate Law Performance

In the previous section, a rate law was developed and calibrated to predict the lead shock particle velocity evolution during the SDT process for PBX 9502. The full rate law is

$$\begin{cases} du_p/dt = 19.0e^{-7.70/u_p} & 0 \le u_p < u_{p,s} \\ du_p/dt = 119.5e^{-7.70/u_p} & u_{p,s} \le u_p \\ \text{with } u_{p,s} = 0.052 - 0.974\, u_{p,0} \end{cases} \tag{6}$$

where $u_{p,0}$ is u_p immediately behind the lead shock at $t = 0$. This rate law is graphically illustrated in Fig. 12.

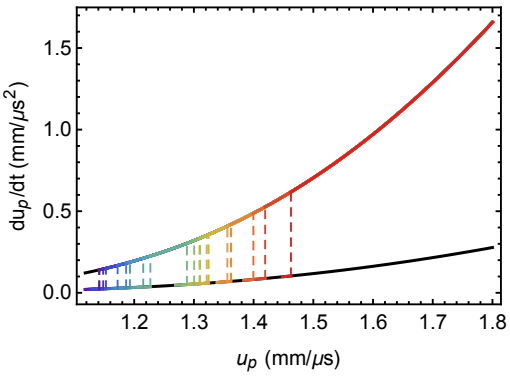

Figure 12: Graphical illustration of the rate law for all tests. Blue-to-red color indicates increasing initial u_p value. Dashed lines indicate $u_{p,s}$ when switching from the lower to higher rate for each test.

A key motivator for the study of Gustavsen et al. [21] was to determine if the microstructural variations associated with differences in the explosive formulation process modified the detonation initiation behavior. The tests spanned explosive that was formulated in four different groups or "lots": V890-005, V890-022, R891-004, and R891-005. Each had different particle morphologies and storage histories as detailed in Gustavsen et al. [21]. Gustavsen et al. [21] reported no detectable variation in SDT behavior across the lots tested, though re-examination of their data shows this to not be the case. Figure 10 of Gustavsen et al. [21] summarizes the time to detonation for each experiment, with the points colored by lot. It can be seen that Lot V890-005 undergoes SDT more rapidly, with all points systematically below the fitted trend. Similarly, all points for Lot R891-004 are above the fitted trend, indicating systematically slower SDT behavior for that lot. Further quantification of the variations present in Gustavsen et al. [21] is beyond the present scope and deferred to future work, but the existence of lot-to-lot variations in the SDT behavior is relevant to the below discussion.

The results of the rate law when using $u_{p,0} = u_{p,1}^{i,fit}$ in the model are shown for explosive from each lot in Figs. 13–16. The markers in each plot are scaled to approximate ± 0.025 mm/μs uncertainty in u_p. The model performance is seen to be good, with the curves intersecting almost all of the markers. The average error per test (normalized by the number of data points per test) is plotted as a function of $u_{p,1}^{expt}$ in Fig. 17 with positive error indicating faster experimental particle velocities relative to the model predictions. The points in the figure are colored according the to the explosive lot, with Lots V890-005, V890-022, R891-004,

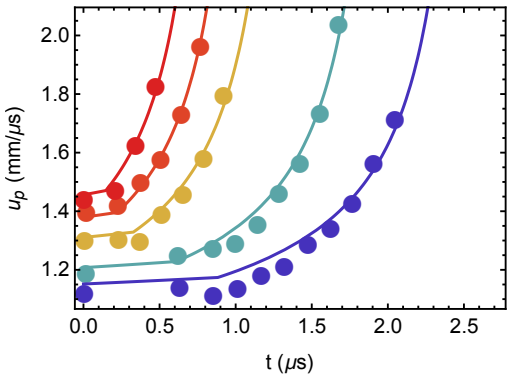

Figure 13: Comparison of rate model to tests with Lot V890-005. Blue-to-red color indicates increasing initial u_p value.

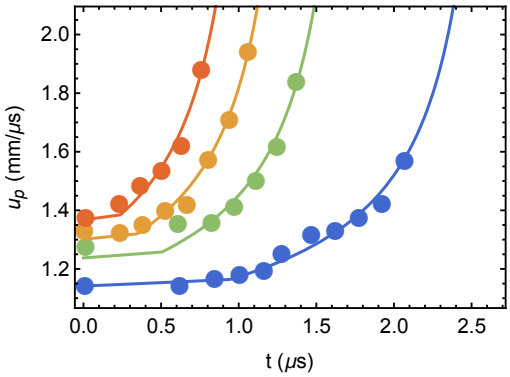

Figure 14: Comparison of rate model to tests with Lot V890-022. Blue-to-red color indicates increasing initial u_p value.

and R891-005 shown as blue, green, orange, and red, respectively. The average percent error for each lot is -0.98% for Lot V890-005, 0.58% for Lot V890-022, -0.10% for Lot R891-004, and -0.10% for Lot R891-005. As with the results of Gustavsen et al. [21], systematic errors are observed. The model appears to systematically overpredict results for Lot V890-005 and slightly underpredict results for Lot V890-022. The systematic nature of these errors indicates slight differences in the rate law constants for each lot. Thus, it is expected that fitting each lot individually could improve the results and provide insight into rate law variations across each lot. This is not pursued here for three reasons. First, the main focus of the present study is to demonstrate the existence of such a rate law for this high explosive. Secondly, the variations across lots are small. Finally, the

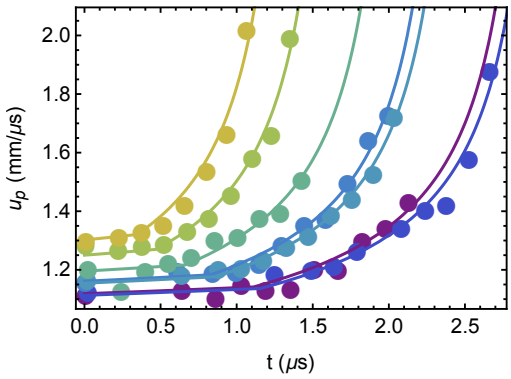

Figure 15: Comparison of rate model to tests with Lot R891-004. Blue-to-red color indicates increasing initial u_p value.

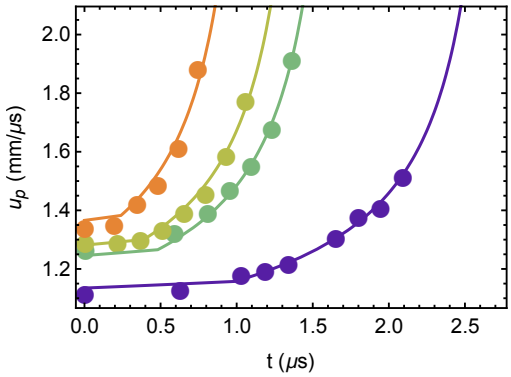

Figure 16: Comparison of rate model to tests with Lot R891-005. Blue-to-red color indicates increasing initial u_p value.

explosive lot histories of Gustavsen et al. [21] convolve variations in formulation and storage history, which make it impossible to attribute any observed rate law variations conclusively to either variable.

4.1. Pop plot prediction

This rate law can also be used to estimate the time to detonation t_p versus the initial shock pressure P_0. This relationship is referred to as the "Pop" plot time after A. Popolato, one of the researchers who discovered it [26]. Figure 18 plots the time t_p versus P_0 for the model (curve) versus the experimental data. The open markers use t_p and P_0 as given by Table 2 in Gustavsen et al. [21]. The closed markers use t_p from Gustavsen et al. [21] with P_0 as computed from the initial

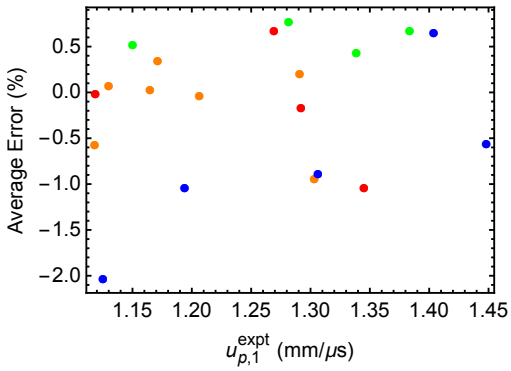

Figure 17: Model error for each test. Colors represent explosive lots as discussed in the text.

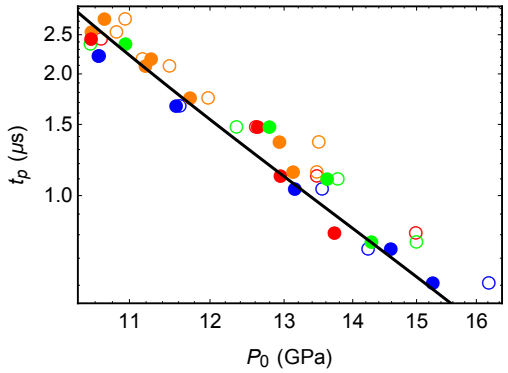

Figure 18: Pop plot data. Open circles are t_p–P_0 values from Table 2 in Gustavsen et al. [21]. Circles use P_0 values as determined in the present work. Colors represent explosive lots as discussed in the text.

explosive densities and shock particle velocity measured in this work, $u_{p,1}^{i,expt}$, via

$$P = \rho_0 u_p \left(c_0 + s u_p\right) \tag{7}$$

which is derived from the momentum conservation law,

$$P = \rho_0 U_s u_p \tag{8}$$

and a linear equation of state

$$U_s = c_0 + s u_p \tag{9}$$

with constant parameters $c_0 = 2.97$ mm/μs and $s = 1.81$ as calibrated by Gustavsen et al. [21]. The P_0 values from the present study are generally lower than

those selected by Gustavsen et al. [21] as the present $u_{p,1}^{i,expt}$ selection approach selects actual measured data points and does not extrapolate using the Hugoniot intersection method described in Fig. 8 of Gustavsen et al. [21]. The model curve was computed by integrating Eq. 4 across a range of $u_{p,0}$ values, assuming a constant $\rho_0 = 1.890$ g/cc and that detonation onset occurred when the solution reached a critical $u_{p,c}$ value of 1.987 mm/μs, which was determined via numerical optimization to best fit the data. This $u_{p,c}$ value is seen to predict the pop plot relationship quite well. Additionally, it is consistent both with the observation that all experimental data with u_p above 2.0 mm/μs appears as a detonation-characteristic profile and that the fitted parameters of Eq. 2 indicate that $u_{p,s} - u_{p,0}$ = 0 for $u_{p,0}$ = 2.018 mm/μs. These multiple correlations suggest that $u_p \approx 2.0$ mm/μs is a critical value for the onset of shock and reaction zone coupling necessary for detonation to occur in PBX 9502.

4.2. Pressure-Dependent Rate Law

The above rate law is also reported as a function of pressure since many reactive flow models use pressure-dependent rate laws. Pressure P can be substituted for u_p in Eq. 4 using Eqs. 8 and 9 to yield

$$\begin{cases} dP/dt = \rho_0 A_L \sqrt{c_0^2 + 4sP/\rho_0}\ \exp\left(-\frac{2sE_{up}}{\sqrt{c_0^2+\frac{4sP}{\rho_0}}-c_0}\right) & 0 \le P < P_s \\ dP/dt = \rho_0 A_H \sqrt{c_0^2 + 4sP/\rho_0}\ \exp\left(-\frac{2sE_{up}}{\sqrt{c_0^2+\frac{4sP}{\rho_0}}-c_0}\right) & P_s \le P \end{cases} \tag{10}$$

with

$$P_s = \rho_0 \left(s\, m(P_0, \rho_0) + c_0\right) m(P_0, \rho_0) \tag{11}$$

and

$$m(P_0, \rho_0) = \left(\frac{0.4871 \left(\sqrt{c_0^2 + \frac{4sP_0}{\rho_0}} - c_0 \right)}{s} + 0.05201 \right) \tag{12}$$

The constants A_L, A_H and E_{up} for the above equation are all identical to those in Section 3.3 since direct substitution was used, while c_0 and s also correspond to their above values. Thus, this formulation yields pre-exponential and activation energy terms that are functions of pressure and density.

The form of Eq. 10 is somewhat onerous and a more compact form can be generated by repeating the fitting process described in Section 3 in pressure space.

The postshock u_p values can be transformed to postshock pressures using Eq. 9 and calibrated to yield

$$\begin{cases} dP/dt = B_L e^{-E_p/P} & 0 \leq P < P_s \\ dP/dt = B_H e^{-E_p/P} & P_s \leq P \end{cases} \tag{13}$$

where B_L = 66.8 GPa/μs, B_H = 553.0 GPa/μs, E_P = 61.9 GPa, and

$$P_s = 0.508 + 0.982 P_0 \quad \text{in GPa.} \tag{14}$$

This more concise form is nearly equivalent to Eq. 10 with consistent performance, but yields a constant pre-exponentials B and activation pressure E_p terms.

5. Discussion

The shock initiation process has long been thought to exhibit multiple stages due to the mesoscale shock and combustion dynamics associated with heterogenous solid explosives. Shock processing of heterogenous explosive microstructure is expected to generate "hotspot" regions of locally high temperature, that lead to localized ignition centers behind the shock front [28, 29]. The subsequent merging and "growth" of those localized reactions leads to a bulk reaction that then fully consumes the reactant. Multiple ignition mechanisms have been proposed and while the full process has never been directly observed in a solid explosive [11], there is a substantial amount of indirect evidence supporting this hypothesized process. For example, heterogenities in liquid explosives have been observed to locally induce igintion [30]. Also, polycrystalline PETN, a solid explosive with a highly heterogenous microstructure, undergoes SDT [31] much more quickly than homogenous single crystals of PETN [32] for comparable shock pressures.

Reactive flow models such as the Ignition and Growth model [3] and subsequent derivatives, as described by Menikoff and Shaw [6], all use this notion of multiple reaction rates to separately model an initially low rate reaction, generally termed "ignition", followed by a higher rate "growth" phase. Additional detail on each model is provided in a recent review [8]. While these models have been quite successful in predicting reaction propagation behind shock waves, prior experimental measurements have never directly revealed the form the reaction rate relationship. Rather, empirical rate functions are proposed in each model and then adjusted to fit experimental data.

This work uses experimental data to directly infer the existence of two distinct reaction rates in the SDT process for PBX 9502, to quantify the time that each rate

influences the wave acceleration, and to quantify the influence of those rates on the shock strength growth during SDT. The trajectory of the latter stage, higher rate trend in Fig. 9 is clearly consistent with a stretched Arrhenius rate form $Ae^{(E_a/P)^n}$. The form of the early time, lower rate is less distinct in the present study due to the relatively large influence of experimental noise relative to the low growth rate and the short duration of time spent in that rate by the wave. However, the adherence of the early time rate to a similar form was supported by the data yielding a similar E_a value to that of the high rate when fitted as an Arrhenius form. These observations support the notion of a two-rate reaction model based on an Arrhenius form such as $Ae^{(E_{up}/u_p)^n}$ or $Ae^{(E_p/P)^n}$.

It is noted that the proposed rate forms in the present work are only intended to predict the acceleration profile of the shock front during the SDT process. It does not predict the evolution of the particle velocity trajectories with increasing distance behind the shock front, nor should it as this data was not used in the calibration methodology. Individual gauge records instead rise to slightly higher values than predicted by the rate law shortly after shock passage before rapidly decaying (Fig. 3). Chemical reaction in this region also occurs and progressively converts the reactants to products. That said, it is expected that the proposed combination of the proposed low rate form, high rate form, and initial-shock-dependent switchover condition could be used to model these features well with recalibrated constants via numerical analysis in a computational fluid dynamic (CFD) reactive model.

6. Conclusions

This work provides the first direct measurement of commonalities in the acceleration profiles of experimental shock motion during the shock-to-detonation transition (SDT) process and provides insight into the functional form of the reaction rate laws for PBX 9502 high explosive. Analysis of the shock motion was found to exhibit a common trend in the shock acceleration–velocity regime. The relationship was observed to be linear in an Arrhenius plot format, indicating that the functional form of the wave acceleration trajectories was consistent with a particle-velocity-dependent or pressure-dependent Arrhenius form. An early-time low-rate transient was also present in the data whose duration was observed to be inversely related to the initial shock strength.

The observed relationship was found to be fit well by a dual-rate particle-velocity-dependent Arrhenius rate law. The rate law had an initial lower rate component for a short time duration before switching to a higher rate component. An

equivalent pressure-dependent Arrhenius rate law was also fit to the data. Integration of the rate law was able to predict both the observed wave motion during the SDT process and the pop plot time-to-detonation relationship. The observation that the initial lower acceleration rate was dependent on the initial shock strength was associated with ignition and merging of hotspots in the high explosive microstructure. The higher acceleration rate was related to progression of a bulk reaction front though the explosive, occurring after the individual hotspots had merged. This relationship is expected to provide insight into developing more physically appropriate forms for rate laws governing high explosive reaction rates.

References

[1] M. Rice, R. McQueen, J. Walsh, Compression of solids by strong shock waves, in: Solid state physics, vol. 6, Elsevier, 1–63, 1958.

[2] S. Jackson, Scaling of the detonation product state with reactant kinetic energy, Combustion and Flame 190 (2018) 240–251.

[3] E. Lee, C. Tarver, Phenomenological model of shock initiation in heterogeneous explosives, The Physics of Fluids 23 (12) (1980) 2362–2372.

[4] B. Wescott, D. Stewart, W. Davis, Equation of state and reaction rate for condensed-phase explosives, Journal of applied physics 98 (5) (2005) 053514.

[5] C. Handley, The CREST Reactive Burn Model, in: Proceedings of the 13th International Detonation Symposium, Office of Naval Research, 864–870, 2006.

[6] R. Menikoff, M. Shaw, Reactive burn models and ignition & growth concept, in: EPJ web of conferences, vol. 10, EDP Sciences, 00003, 2010.

[7] T. Aslam, Shock temperature dependent rate law for plastic bonded explosives, Journal of Applied Physics 123 (14) (2018) 145901.

[8] C. Handley, B. Lambourn, N. Whitworth, H. James, W. Belfield, Understanding the shock and detonation response of high explosives at the continuum and meso scales, Applied Physics Reviews 5 (1) (2018) 011303.

[9] C. Tarver, T. Tran, Thermal decomposition models for HMX-based plastic bonded explosives, Combustion and Flame 137 (1-2) (2004) 50–62.

[10] S. Son, H. Berghout, C. Bolme, D. Chavez, D. Naud, M. Hiskey, Burn rate measurements of HMX, TATB, DHT, DAAF, and BTATz, in: Symposium (International) on Combustion, vol. 1, 919–924, 2000.

[11] A. Campbell, W. Davis, J. Ramsay, J. Travis, Shock initiation of solid explosives, The Physics of Fluids 4 (4) (1961) 511–521.

[12] M. M. Cowperthwaite, Determination of energy-release rate with the hydrodynamic properties of detonation waves, in: Symposium (International) on Combustion, vol. 14, Elsevier, 1259–1264, 1973.

[13] M. M. Cowperthwaite, Characterization of initiation and detonation by Lagrange gage techniques. Final report, Tech. Rep. UCRL-15482, SRI International, Prepared for LLNL, doi:doi:10.2172/7057230, 1982.

[14] H. Vantine, R. Rainsberger, W. Curtis, R. Lee, M. Cowperthwaite, J. Rosenberg, Accuracy of reaction rates inferred from Lagrange analysis and in-situ gauge measurements, in: Proceedings of the Seventh International Detonation Symposium, Office of Naval Research, 466–478, 1981.

[15] C. Forest, Lagrangian analysis, data covariance, and the impulse time integral, in: Shock Compression of Condensed Matter 1991, Elsevier, 317–324, 1991.

[16] C. Handley, Lagrangian analysis of velocity gauge data to determine reaction rate histories in EDC37, in: AIP Conference Proceedings, vol. 845, AIP, 1073–1076, 2006.

[17] R. Winter, S. Sorber, D. Salisbury, P. Taylor, R. Gustavsen, S. Sheffield, R. Alcon, Experimental study of the shock response of an HMX-based explosive, Shock Waves 15 (2) (2006) 89–101.

[18] S. Sorber, R. Gustavsen, S. Sheffield, R. Alcon, B. Bartram, Analysis of Shock Wave and Initiation Data for Solid Explosives, in: Proceedings of the Fourteenth International Detonation Symposium, Office of Naval Research, 573–582, 2010.

[19] T. Gibbs, A. Popolato, LASL Explosive Property Data, University of California Press, 1980.

[20] S. I. Jackson, M. Short, Scaling of detonation velocity in cylinder and slab geometries for ideal, insensitive and non-ideal explosives, J. Fluid Mech. 773 (2015) 224–266.

[21] R. Gustavsen, S. Sheffield, R. Alcon, Measurements of shock initiation in the tri-amino-tri-nitro-benzene based explosive PBX 9502: Wave forms from embedded gauges and comparison of four different material lots, Journal of Applied Physics 99 (11) (2006) 114907.

[22] P. D. Peterson, D. J. Idar, Microstructural differences between virgin and recycled lots of PBX 9502, Propellants, Explosives, Pyrotechnics: An International Journal Dealing with Scientific and Technological Aspects of Energetic Materials 30 (2) (2005) 88–94.

[23] L. Hill, T. Aslam, Detonation Shock Dynamics Calibration for PBX 9502 with Temperature, Density, and Material Lot Variations, in: Proceedings of the Fourteenth International Detonation Symposium, Office of Naval Research, 779–788, 2010.

[24] J. Bdzil, T. Aslam, R. Henninger, J. Quirk, High-explosives performance, Los Alamos Sci 28 (2003) 96.

[25] S. Sheffield, R. Gustavsen, R. Alcon, In-situ magnetic gauging technique used at LANL-method and shock information obtained, in: AIP Conference Proceedings, vol. 505, AIP, 1043–1048, 2000.

[26] J. Ramsey, A. Popolato, Analysis of shock wave and initiation data for solid explosives, in: Proceedings of the Fourth International Detonation Symposium, Office of Naval Research, 233–238, 1965.

[27] T. D. Aslam, The reactants equation of state for the tri-amino-tri-nitrobenzene (TATB) based explosive PBX 9502, Journal of Applied Physics 122 (3) (2017) 035902.

[28] H. Eyring, R. E. Powell, G. H. Duffy, R. B. Parlin, The Stability of Detonation., Chemical Reviews 45 (1) (1949) 69–181.

[29] F. P. Bowden, A. D. Yoffe, Initiation and growth of explosion in liquids and solids, CUP Archive, 1985.

[30] A. Campbell, W. Davis, J. Travis, Shock initiation of detonation in liquid explosives, The Physics of Fluids 4 (4) (1961) 498–510.

[31] G. Seay, L. S. Jr., Initiation of a low-density PETN pressing by a plane shock wave, Journal of Applied Physics 32 (6) (1961) 1092–1097.

[32] J. Dick, Effect of crystal orientation on shock initiation sensitivity of pentaerythritol tetranitrate explosive, Applied Physics Letters 44 (9) (1984) 859–861.

Appendix A. Data Table

Table A.1: Test details. Test identifier, lot, initial density, initial shock pressure and pop plot time as reported by Gustavsen et al. [21]. Also shown are measured and fitted postshock values at the lead gauge, their percent difference, and the corresponding fitted postshock pressure value.

Test	Lot	ρ_0 (g/cc)	P_0 (GPa)	t_p (μs)	$u_{p,1}^{expt}$ (mm/μs)	$u_{p,1}^{fit}$ (mm/μs)	$u_{p,1}^{fit}/u_{p,1}^{expt} - 1$ (%)	P_1^{fit} (GPa)
2s-058	R891-004	1.892	10.85	2.55	1.118	1.118	+0.04	10.89
2s-117	R891-005	1.889	10.67	2.45	1.119	1.135	+1.44	11.08
2s-070	V890-005	1.889	10.65	2.22	1.125	1.152	+2.36	11.31
2s-044	R891-004	1.890	10.95	2.75	1.13	1.113	-1.49	10.81
2s-136	V890-022	1.886	10.55	2.38	1.15	1.142	-0.71	11.17
2s-068	R891-004	1.893	11.49	2.10	1.165	1.161	-0.300	11.42
2s0-42	R891-004	1.890	11.16	2.18	1.171	1.154	-1.43	11.33
2s-069	V890-005	1.889	11.62	1.67	1.194	1.208	+1.14	12.04
2s-041	R891-004	1.890	11.98	1.75	1.206	1.195	-0.89	11.86
2s-116	R891-005	1.891	12.61	1.48	1.269	1.246	-1.84	12.55
2s-134	V890-022	1.888	12.35	1.48	1.282	1.238	-3.41	12.44
2s-057	R891-004	1.889	13.50	1.36	1.291	1.250	-3.16	12.61
2s-114	R891-005	1.889	13.47	1.12	1.292	1.281	-0.80	13.04
2s-040	R891-004	1.891	13.47	1.15	1.303	1.302	-0.08	13.35
2s-086	V890-005	1.888	13.55	1.04	1.306	1.311	+0.33	13.46
2s-118	V890-022	1.887	13.78	1.10	1.339	1.301	-2.78	13.33
2s-115	R891-005	1.889	14.99	0.81	1.345	1.366	1.56	14.27
2s-119	V890-022	1.887	15.00	0.77	1.383	1.368	-1.12	14.29
2s-043	V890-005	1.887	14.24	0.74	1.404	1.380	-1.71	14.47
2s-085	V890-005	1.886	16.22	0.61	1.448	1.456	+0.57	15.64